Tissue Dissection with Ultrafast Laser using Extended and Multiple Foci

I. Toytman*[a], A. Silbergleit[a], D. Simanovski[a], D. Palanker[a,b]
[a] Hansen Experimental Physics Laboratory,
[b] Department of Ophthalmology,
Stanford University, Stanford, CA 94305

ABSTRACT

Ultrashort lasers are typically utilized for tissue dissection by sequential application of tightly focused beam along a scanning pattern. Each pulse creates a small (on the order of 1μm) zone of multiphoton ionization (optical breakdown). At energies exceeding vaporization threshold cavitation bubble is formed around the focal volume. A continuous cut is formed if the rupture zones produced by separate bubbles coalesce. We present an alternative approach, in which an extended zone of tissue is cut by simultaneous application of laser energy in multiple foci. Simultaneous formation of multiple cavitation bubbles results in hydrodynamic interactions that can lead to significant extension of the rupture zone in tissue. Two simultaneously expanding bubbles compress and strain material between them, while simultaneously collapsing bubbles can produce jets towards each other.

We calculated and experimentally imaged the flow dynamics of expanding and collapsing bubbles and obtained maps of tissue deformation. With the measured tissue threshold strain, the deformation map allows predicting the rupture zone as a function of maximum bubble size and distance between the bubbles.

We also demonstrate an optical system producing 1 mm long dissection with a single laser pulse. A combination of a lens and an axicon produces a line of optical breakdown, with aspect ratio 250:1. The subsequent cavitation bubble has aspect ratio 100:1 at early stage of expansion. We calculated an optimal laser beam intensity profile to create axially-uniform elongated ionization pattern.

Keywords: ultrafast laser, optical breakdown, axicon, cavitation

1. INTRODUCTION

Ultrafast lasers have become a common tool for a variety of biomedical applications. They are now widely used in ophthalmology for creating corneal flap during LASIK surgery, replacing less precise mechanical microkeratome. High precision of corneal cuts created by femtosecond lasers is also useful for keratoplasty [1]. Another recent development in the use of ultrafast lasers in ophthalmology is associated with making incisions in a crystalline lens. It has been shown that femtosecond lasers can perform anterior capsulotomy and lens fragmentation for cataract removal [2]. In addition, softening the crystalline lens by patterned incisions could provide a means for presbyopia treatment [3]. Several cellular-scale applications of ultrafast lasers have been demonstrated including dissection of a single neuron [4] and excision of an area of interest in a histological preparation [5]. Femtosecond pulses are capable of targeting and cutting the subcellular structures such as chromosomes [6], mitochondria [7], and plant plastids [8] without damaging surrounding cellular organelles, thereby maintaining cell viability. Cellular membrane can also be perforated for DNA delivery [9].

In all these applications laser pulses are applied sequentially. Each pulse creates plasma in a focal zone within the sample as a result of multiphoton absorption and impact ionization. At certain density this plasma becomes highly absorbing for the laser radiation, which results in rapid heating and subsequent explosive vaporization of the tissue within the focal zone. In liquids this is followed by a cavitation bubble that mechanically ruptures the sample. The size of the resulting rupture zone sets the limit to maximum separation between subsequent pulses for producing a continuous cut.

Sequential approach allows producing cuts of arbitrary three-dimensional shapes. However, it could be hindered by transient cavitation bubbles or residual gas bubbles that do not dissolve until after few seconds [10] and therefore may alter focusing conditions for subsequent pulses. Furthermore, precise apposition of sequential laser pulses in ophthalmic

applications can be difficult due to constant eye movement, while poor visibility of the cellular membrane may hinder its poration.

We studied a possibility of enhancement of tissue dissection using hydrodynamic interactions between two simultaneously produced cavitation bubbles, and calculate the extent of the resulting rupture zone as a function of separation between the bubbles and mechanical parameters of the material. We compare the rupture zones produced by simultaneous and by sequential pulses, and evaluate the total energy required for a continuous cut. Alternative approach to extension of the cutting zone also presented in this work is based on producing a highly elongated region of optical breakdown using a single laser pulse focused by a combination of an axicon and a lens.

2. ANALYTICAL DESCRIPTION OF HYDRODYNAMIC INTERACTIONS BETWEEN TWO EXPANDING BUBBLES

Consider a single spherical bubble that expands within an incompressible fluid from radius R_1 to R_2. An arbitrary point at a distance $r_1 > R_1$ from the bubble center will, upon bubble expansion, be located at the distance r_2. From the incompressibility condition, the volume of material confined by spheres of radii R_1 and r_1 before the bubble expansion should be equal to that confined by spheres of radius R_2 and r_2 after the expansion. Therefore, we can calculate the displacements r_2-r_1:

$$r_2 - r_1 = \sqrt[3]{r_1^3 - R_1^3 + R_2^3} - r_1 \tag{1}$$

Deformations of a continuous body can be characterized by the strain tensor. It is well known that the deformation of an infinitesimally small volume can be decomposed into three independent deformations, each of them being either simple stretching or compression along mutually orthogonal axes known as principle axes. In these axes the strain tensor has only diagonal components (eigenvalues of the tensor); we assume that the material is ruptured if the magnitude of at least one of them exceeds certain threshold ε_{th}. Thus, we are interested in largest eigenvalue of the strain tensor, which we will call simply "strain", for brevity. It can be shown that in our case the strain ε at a point r_1 is

$$\varepsilon(r_1) = \frac{r_2 - r_1}{r_1} = \sqrt[3]{1 + \frac{R_2^3 - R_1^3}{r_1^3}} - 1, \tag{2}$$

thus the rupture zone radius, $R_{rupture}$, is found to be:

$$R_{rupture} = \sqrt[3]{\frac{R_2^3 - R_1^3}{(1+\varepsilon_{th})^3 - 1}} \tag{3}$$

The above argument works for a single bubble only. For any number of bubbles the displacements can be determined by solving the proper boundary value problem (BVP) about the flow of an incompressible inviscid fluid due to adiabatic expansion of initially spherical gas bubbles. The flow is potential, with the potential, Φ, obeying the Laplace equation:

$$\Delta\Phi = 0 \tag{4}$$

and the boundary conditions:

$$\left.\frac{\partial\Phi}{\partial\vec{n}}\right|_S = v_{boundary}$$
$$P_{gas} = p_{boundary} \tag{5}$$

Here S and $v_{boundary}$ represent the shape and the velocity of the boundary of each bubble, P_{gas} is the gas pressure inside the bubble, and $p_{boundary}$ is the pressure of the liquid immediately at the bubble boundary. The latter is expressed through the potential using the Bernoulli integral:

$$\rho\left[\frac{\partial\Phi}{\partial t}+\frac{1}{2}(\nabla\Phi)^2\right]_S + p_{boundary} = p_\infty \tag{6}$$

where p_∞ is the hydrostatic pressure and ρ is the liquid density.

A single bubble is the simplest case of this nonlinear BVP, since the boundary shape is known: the bubble remains spherical, with only its radius changing. This allowed Rayleigh [11] (see also [12]) to find a simple exact solution: the potential is just a 0-th order multi-pole whose strength ('charge') is changing with the time.

Basing on this, in the case of two bubbles we represent the flow potential as a superposition of axially symmetric multi-poles in two spherical coordinate systems with the origins at the centers of the bubbles, simultaneously expanding the unknown, except at the initial time, shapes of their boundaries as functions of the corresponding polar angles. So our *Anzatz* for the solution to the second order is:

$$\Phi(r,\theta,t)=\frac{A_1(t)}{r_1}+\frac{A_2(t)}{r_2}+\frac{B_1(t)P_1(\cos\theta_1)}{r_1^2}+\frac{B_2(t)P_1(\cos\theta_2)}{r_2^2}+\frac{C_1(t)P_2(\cos\theta_1)}{r_1^3}+\frac{C_2(t)P_2(\cos\theta_2)}{r_2^3} \tag{7}$$

$$R(\theta,t)=a(t)+\alpha(t)P_1(\cos\theta)+\beta(t)P_2(\cos\theta) \tag{8}$$

where A, B, C, a, α, and β are the functions to be found, $P_1(x)$ and $P_2(x)$ are the Legendre polynomials, indices 1 and 2 denote the coordinates in the system centered at the first and the second bubble, respectively, and $R(\theta, t)$ describes the shape of each bubble. Note that to lowest order solution (7) is a superposition of the monopoles giving the exact solution for either of the two bubbles in the absence of the other one. We assume that the distance between bubbles is large enough to consider the effect of the second bubble as a perturbation to the flow produced by the first one, and, accordingly, that the deviations of the boundary shape from the spherical one are relatively small. This allows for a perturbative solution resulting in explicit expressions (in terms of some quadratures) for all the unknown functions of time.

Knowing the flow velocity distribution at any given moment of time the displacements can be calculated either analytically or numerically. We have chosen and implemented the following numerical procedure. The entire bubble expansion time was divided into 1000 equal intervals Δt, and the flow within each interval was approximated by that in the beginning of the interval. The trajectory of any arbitrary point could then be iteratively constructed, with each iteration consisting of calculating the velocity v of the point and then adding the displacements $v*\Delta t$ to the current point coordinates.

To find strain at a given point A we calculate the displacement of A as well as the displacements of three points located at distance L/1000 away from A along three perpendicular directions, where L is the distance between the bubbles. The strain tensor components are obtained by replacing the derivatives in their definitions with finite differences, and the value of the strain is obtained by computing the largest of eigenvalues of the strain tensor. Rupture zones for materials with various ε_{th} at maximum bubble expansion and after bubble collapse are shown in Fig. 1a-b.

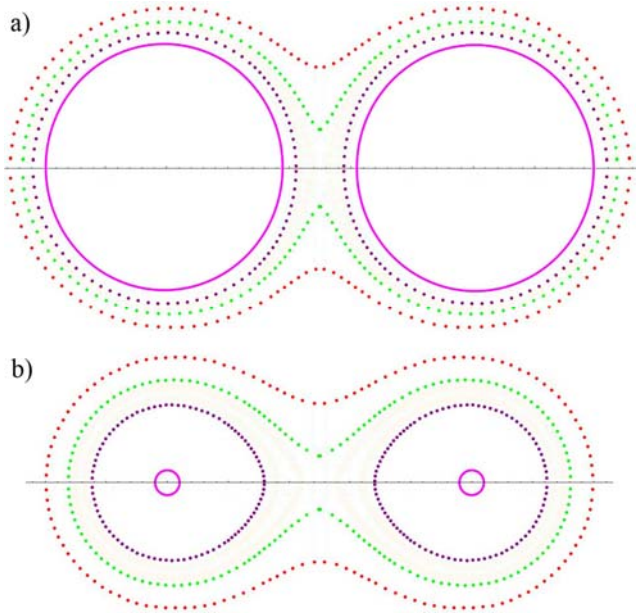

Fig. 1. Rupture zones produced by two simultaneously created bubbles: a) at maximum bubble expansion; b) after the bubble collapse. Solid line – bubble contours; red, green, purple – rupture zones for materials with ε_{th}=0.3, ε_{th}=0.5, and ε_{th}=1, respectively.

3. EXPERIMENTAL SETUP

Two simultaneous points of laser induced breakdown can be produced by focusing two laser beams with a single microscope objective. Focal spots could be separated axially and laterally by independent adjustment of the divergence and angle of incidence for each beam (Fig. 2a-b). We found that in our setup beams with different divergence produced slightly different cavitation bubbles, while tilted beams produced very similar initial spherical bubbles. Therefore, for the sake of consistency, we have chosen scheme with laterally separated bubbles where distance between the bubbles could be tuned by changing the angle φ.

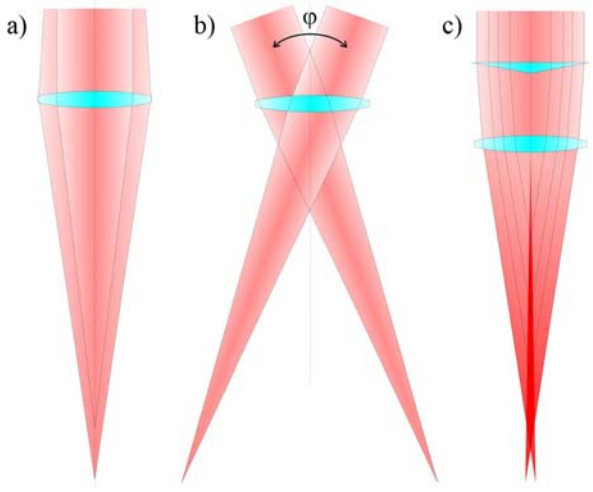

Fig. 2. Focusing geometries for creating two cavitation bubbles: with axial (a) and lateral (b) separation; and for creating optical breakdown in a highly elongated region (c).

We used Ti:Sapphire laser (1mJ, 1ps, 800nm) operated at 10Hz repetition rate, and single pulses were selected by a mechanical shutter. Pulse energy was adjusted by a variable attenuator consisting of a half-wave plate and a polarizer.

Following the attenuator, the pulse was split by a thin-film polarizer (TFP). Another half-wave plate was introduced in front of the TFP to ensure equal distribution of energy between two resulting pulses. Focusing system with large numerical aperture is essential to avoid self focusing effect in water and to produce well localized focal spots and highly spherical bubbles. We used a 63x water-immersion objective (Zeiss, NA=0.9). To study optical breakdown in a high aspect ratio regime TFP and the second half-wave plate were removed and the focusing objective was replaced with a 10x Olympus UMPlanFL (NA=0.3). High aspect ratio of focal volume was achieved by placing an axicon (refractive index n = 1.45, apex angle $\alpha = 179°$) in front of the objective (Fig. 2c).

Cavitation bubbles were produced in water and imaged with fast flash photography. The imaging system consisted of a 10x microscope objective (Nikon, NA=0.3), a 250mm field lens, and a CCD camera (Photometrics CoolSnapHQ). Water was held in a glass cuvette made of thin (170μm) glass slides to allow for imaging through its walls with minimized aberrations. The flash was provided by an LED synchronized with the laser by a variable delay generator. The LED light was focused onto the sample by a lens matching the NA of the imaging objective. Flash of up to 100ns duration could be obtained by driving the LED with a short pulse of high voltage (1.5kV). It was also possible to obtain time-integrated image by increasing the flash duration up to 1ms.

Threshold strain ε_{th} was measured in gelatin with 90% water content (by mass). Top gelatin boundary was made flat and a layer of oil was added on it to facilitate visualization of the boundary. Cavitation bubbles of constant radius were created within gelatin at various distances from the gelatin-oil boundary. When this distance was smaller than the rupture zone, ejection of gelatin into oil upon the bubble expansion could be observed. This way the rupture zone radius could be estimated by the maximum distance between the bubble center and the oil-gelatin boundary, at which the boundary is ruptured. The value of ε_{th} can be derived from the measured radius of rupture zone using Eq. 3.

4. RESULTS AND DISCUSSION

4.1 Experimental verification of theoretically predicted bubble shapes

The validity of the theoretical formulation was verified by comparing the exact solution available for single bubble with images obtained in the experiment. Fig. 3 (top row) shows various stages of evolution of a single spherical bubble – in excellent agreement with overlaid bubble contours computed from the analytical solution. The agreement is slightly worse in case of two bubbles (Fig. 3, bottom row), with the maximum deviation of the predicted contours from the experimental ones being ~20%. The deviation is caused by fairly small distance between the bubbles compared to the maximum bubble radius – a situation, for which perturbation theory might be inaccurate. It is important, however, that our model still describes the central portion of the contours ($\theta < 15°$) very well.

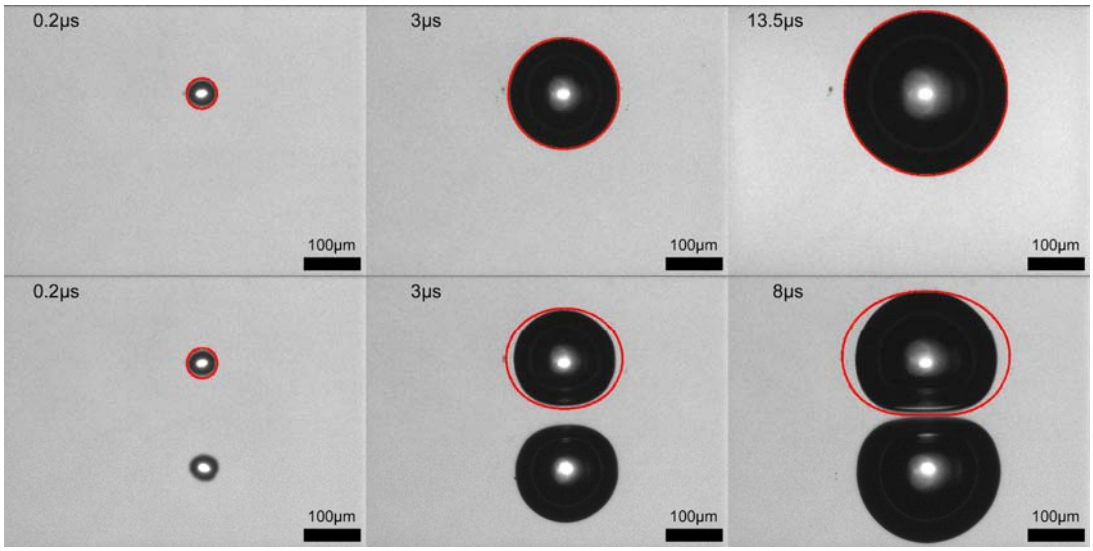

Fig. 3. Analytically calculated bubble contours overlaid on the experimentally observed bubbles in case of single bubble (top row) and two bubbles (bottom row).

For more complex (viscous and elastic) materials such as real biological tissues theoretical model of deformation may not be available. However, in some cases the displacements can be visualized experimentally as demonstrated in Fig. 4. We embedded 1μm polystyrene beads into the gelatin and made a time-integrated image of two bubbles expanding within such sample. The resulting displacements are represented by tracks produced by the beads. By acquiring a number of these images one can in principle obtain an entire map of displacements with the resolution equal to the size of the marker (1μm in our example).

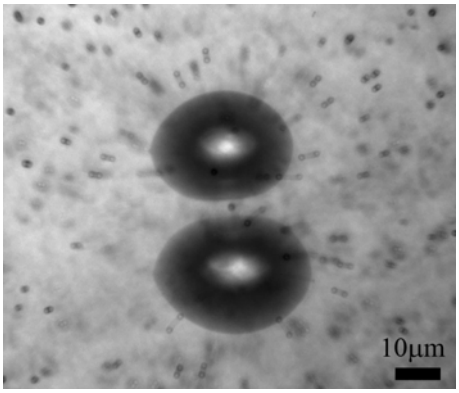

Fig. 4. Displacements of 1μm polystyrene beads in gelatin resulting from the expansion of two cavitation bubbles

4.2 Measurement of threshold strain of gelatin and optimization of the distance between bubbles

Time-integrated images of cavitation bubbles in gelatin at various distances from the gelatin-oil boundary are shown in Fig. 5 (a-c). These images represent three possible scenarios – bubble is far from the boundary (no ejection of gelatin into oil), bubble center is at the distance $R_{rupture}$ from the boundary (very little gelatin is ejected), and bubble is very close to the boundary (significant amount of gelatin is ejected). From Fig. 5b we estimate $R_{rupture}$ and the maximum bubble radius to be 23.5μm and 40μm, respectively, and the corresponding value of $\varepsilon_{th} = 0.7$.

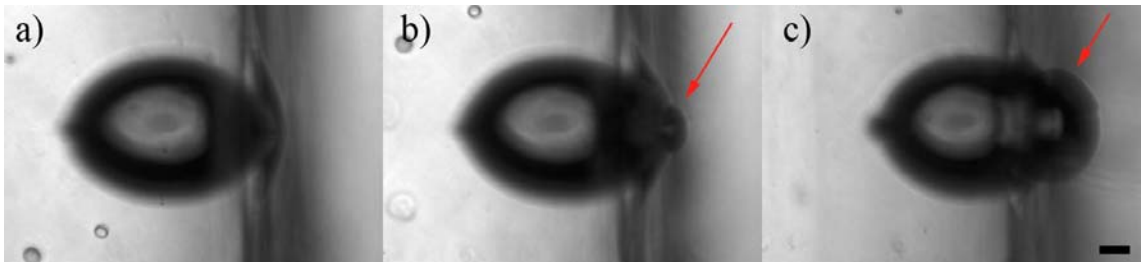

Fig. 5. Cavitation bubble produced in gelatin at various distances from gelatin-oil boundary: a) no boundary rupture; b) minimal boundary rupture; c) profound boundary rupture. Scale bar represents 10μm, arrows point to the ejected portion of gelatin.

For this ε_{th} single bubble with maximum radius R_{max} produces rupture zone of the radius $R_{rupture} = 0.7R_{max}$. The maximum distance between two simultaneously created bubbles that would result in a continuous rupture zone is $L=2.37R_{max}$, which corresponds to a factor of 1.7 increase in length of the rupture zone, comparing to the effect of two sequential bubbles.

4.3 Interaction between two simultaneously collapsing bubbles in liquid

In liquid media two bubbles at a distance ~$2.5R_{max}$ get attracted to each other during the collapse stage, producing colliding jets (Fig. 6). On subsequent rebound the bubbles merge and potentially can break a layer of soft tissue placed in-between. One possible application of this type of interaction is cell poration. When rupturing a membrane with a single bubble originating at small distance from the membrane, the bubble first expands and pushes the membrane away, thereby decreasing the probability of rupture. In contrast to that, membrane located between two simultaneously created bubbles is "trapped" and is more likely to be ruptured by jets produced by the bubbles.

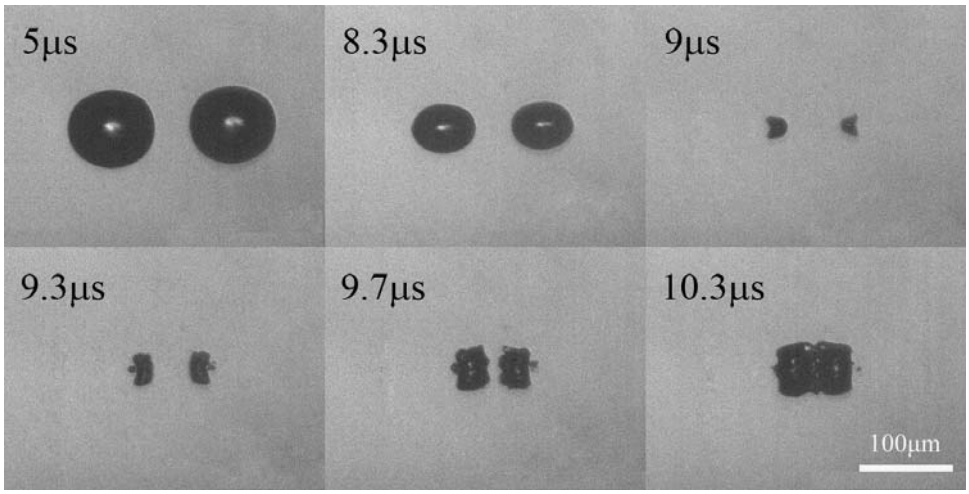

Fig. 6. Attraction of cavitation bubbles in low viscosity liquid (water) at the collapse stage.

4.4 Optical breakdown in the highly elongated region

The intensity distribution produced by a combination of an axicon and a lens was visualized with two-photon fluorescence (Fig. 7). Elongated region of high intensity is clearly visible along the axis and with sufficiently high laser energy plasma could be detected. Due to non-uniform axial intensity distribution of laser pulse plasma is visible only in a part of the entire breakdown region. The length of this region could be estimated from the image of the initial cavitation bubble obtained 100ns after the laser pulse (Fig. 8). For laser pulse energy of 65μJ the breakdown zone length is 1.2mm, and since the maximum plasma width is ~5μm the aspect ratio of the breakdown region exceeds 250:1.

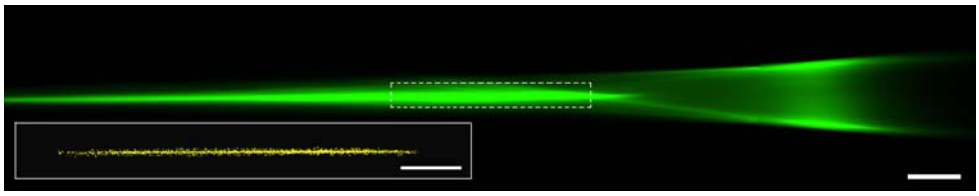

Fig. 7. Two-photon fluorescence induced by a laser pulse focused with a combination of an axicon and a lens. Scale bar represents 100μm. Inset shows visible part of plasma in the region marked by a dashed box. Scale bar in the inset represents 50μm.

Uneven axial intensity distribution leads to non-uniform bubble shape as the bubble evolves. The distal end (further from the axicon) is exposed to higher light intensity and therefore expands for several microseconds, while the other (proximal) end collapses almost immediately (within less than 1μs), as shown in Fig. 8.

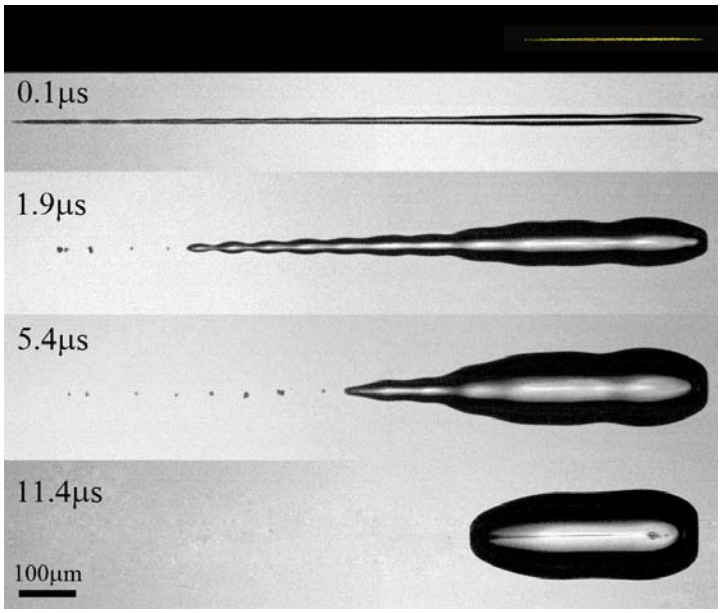

Fig. 8. Visible plasma and evolution of subsequent cavitation bubble.

The axial light intensity produced by the combination of an axicon and a lens can be calculated using Fresnel diffraction theory:

$$I_{axial}(z) = \frac{2E}{\pi w^2}\frac{k^2}{z^2}\left|\int_0^R \exp\left[-\frac{r^2}{w^2} - ik\left(r\sin\theta + \frac{r^2}{2f} - \frac{r^2}{2z}\right)\right] r dr\right|^2 \tag{9}$$

Here ρ and z are cylindrical coordinates of a point of interest, E is the pulse energy, w is the beam waist, k is the magnitude of the wave vector, R is the radius of clear aperture of the axicon, θ is the angle of refraction produced by the axicon, f is the focal length of the lens. The integral can be computed numerically, and the resulting plot of axial intensity as a function of z coordinate for 65μJ pulse energy is shown in Fig. 9a. From the plot the length of the breakdown zone of 1.2mm corresponds to the breakdown threshold intensity of 6mJ/cm^2. The light intensity exceeds the required threshold by a factor of 15 at its maximum, which indicates quite inefficient utilization of the pulse energy and leads to significant widening of the distal end of the bubble. More uniform axial distribution can be produced if an amplitude mask is placed in front of the axicon that would modulate the beam intensity profile. Using stationary phase analysis [13], we could calculate the transmission function of the mask T(r):

$$\begin{cases} T(r) = \dfrac{r_{\min} + f\sin\theta}{r + f\sin\theta}\sqrt{\dfrac{r_{\min}}{r}}\exp\left[\dfrac{r^2}{w^2} - \dfrac{r_{\min}^2}{w^2}\right], & r_{\min} < r < R, \\ T(r) = 0, & \text{otherwise.} \end{cases} \tag{10}$$

Here r_{min} defines the radius of the central opaque region of the mask, and its value determines the location of the proximal end of the breakdown zone. We used r_{min}=0.7mm in order to achieve the breakdown threshold over 1.2mm length (Fig. 9b) – same as in experiment described above. The amount of energy delivered to the sample with the mask is only 16μJ. However, since the mask is highly absorptive it requires significantly higher pulse energy – 165μJ.

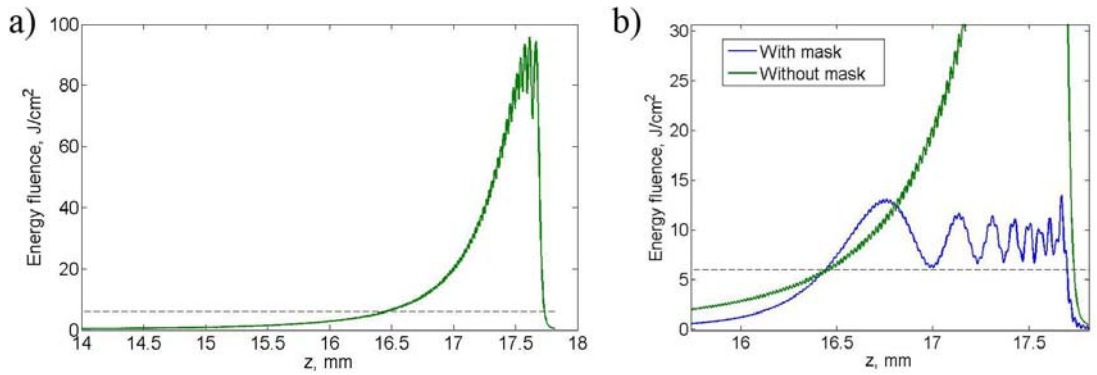

Fig. 9. a) Axial intensity distribution produced by a 65μJ pulse focused with an axicon and a lens; b) Axial intensity distribution with (blue) and without (green) the amplitude mask. Dashed line indicates the dielectric breakdown threshold.

Without an axicon a 16μJ pulse will produce a spherical bubble of 126μm radius. Assuming the same volume of bubble for both geometries, the radius of a cylindrical bubble of L=1.2 mm in length is R=47μm. Therefore, axicon allows for 4.8 times longer cut than a spherical bubble created by the same pulse energy. Assuming that in sequential cutting the bubbles are separated by a radius, a cut of length L will require N=L/R bubbles (N=26 in the current example). Interestingly, the volume of a cylindrical bubble of length L and radius R is similar to the total volume of N=L/R spherical bubbles of radius R. This means that the total amount of energy required for producing a cut of the same length and width with a single cylindrical bubble, and with a series of sequential spherical bubbles separated by a radius is similar.

5. CONCLUSIONS

We have developed a model that predicts displacements and strain induced by two cavitation bubbles adiabatically expanding in incompressible inviscid liquid. Using this model we showed that in gelatin and materials with similar mechanical properties rupture zone can be increased by a factor of 1.7 with two simultaneous cavitation bubbles compared to the sequential approach. For cavitation bubbles in non-viscous materials (such as water) formation of jets during collapse can potentially be used for poration of thin membrane located between them.

We also show optical breakdown in a region with high aspect ratio (250:1) achieved by a combination of an axicon and a lens. Such system allows for instantaneous line incisions, which is advantageous for application to moving targets. We have estimated that similar total energy is required for a cut to be produced with axicon-based and conventional approaches. The laser energy distribution over the breakdown region produced by our system can be further optimized with an amplitude mask with transmission calculated using Fresnel diffraction theory. We plan to verify the performance of such mask in the future.

REFERENCES

[1] Ide, T., Yoo, S. H., Kymionis, G. D., Leng, T., Marini, C., Stanciu, N. A. and O'Brien, T. P., "Descemet stripping automated endothelial keratoplasty tissue preparation with femtosecond laser and contact lens," Cornea 29(1), 93-98 (2010).

[2] Nagy, Z., Takacs, A., Filkorn, T. and Sarayba, M., "Initial clinical evaluation of an intraocular femtosecond laser in cataract surgery," J Refract Surg. 25(12), 1053-1060 (2009).

[3] Ripken, T., Oberheide, U., Fromm, M., Schumacher, S., Gerten, G. and Lubatschowski, H., "fs-Laser induced elasticity changes to improve presbyopic lens accommodation," Graefes Arch Clin Exp Ophthalmol 246(6), 897–906 (2008).

[4] Chung, S. H. and Mazur, E., "Femtosecond laser ablation of neurons in *C. elegans* for behavioral studies," Appl Phys A 96(2), 335–341 (2009).

[5] Tsai, P. S., Friedman, B., Ifarraguerri A. I., Thompson, B. D., Lev-Ram, V., Schaffer, C. B., Xiong, Q., Tsien, R. Y., Squier, J. A. and Kleinfeld, D., "All-optical histology using ultrashort laser pulses," Neuron 39(1), 27-41 (2003).

[6] König, K., Riemann, I. and Fritzsche, W., "Nanodissection of human chromosomes with near-infrared femtosecond laser pulses," Opt. Lett. 26(11), 819-821 (2001).
[7] Shimada, T., Watanabe, W., Matsunaga, S., Higashi, T., Ishii, H., Fukui, K., Isobe, K. and Itoh, K., "Intracellular disruption of mitochondria in a living HeLa cell with a 76-MHz femtosecond laser oscillator," Opt. Express 13(24), 9869-9880 (2005).
[8] Tirlapur, U. K. and König, K., "Femtosecond near-infrared laser pulses as a versatile non-invasive tool for intra-tissue nanoprocessing in plants without compromising viability," Plant J. 31(3), 365-74 (2002).
[9] He, H., Kong, S. K., Lee, R. K., Suen, Y. K. and Chan, K. T., "Targeted photoporation and transfection in human HepG2 cells by a fiber femtosecond laser at 1554 nm," Opt. Lett. 33(24), 2961-2963 (2008).
[10] Krueger, R., Sun, X., Stroh, J., and Myers, R., "Experimental increase in accommodative potential after neodymium:yttrium–aluminum–garnet laser photodisruption of paired cadaver lenses," Ophthalmol. 108(11), 2122-2129 (2001).
[11] Rayleigh, L., "On the pressure developed in a liquid during the collapse of a spherical cavity," Philos. Mag. 34(199), 94-98 (1917).
[12] Plesset, M. S., "The Dynamics of Cavitation Bubbles," Trans. ASME. J. Appl. Mech. 16, 228-231 (1949).
[13] Friberg, A. T., "Stationary-phase analysis of generalized axicons," J. Opt. Soc. Am. A 13(4), 743-750 (1996).